Hybrid energy and angle dispersive X-ray diffraction computed tomography

ASHKAN AJEER,[1,*] JIA C. KHONG,[1] MATTHEW D. WILSON,[2] AND ROBERT M. MOSS[1]

[1]*Department of Medical Physics & Biomedical Engineering, University College London, Gower Street, London, WC1E 6BT, UK*
[2]*Science and Technology Facilities Council, Rutherford Appleton Laboratory, Harwell Campus, Didcot, OX11 0QX, UK*
*a.ajeer@ucl.ac.uk

Abstract: Pixelated energy resolving detectors enable acquisition of X-ray diffraction (XRD) signals using a hybrid energy- and angle- dispersive technique, potentially paving the way for the development of novel benchtop XRD imaging or computed tomography (XRDCT) systems, utilising readily available polychromatic X-ray sources. In this work, a commercially available pixelated cadmium telluride (CdTe) detector, HEXITEC (High Energy X-ray Imaging Technology), was used to demonstrate such an XRDCT system. Specifically, a novel fly-scan technique was developed and compared to the established step-scan technique, reducing the total scan time by 42% while improving the spatial resolution, material contrast and therefore the material classification.

1. Introduction

X-ray diffraction (XRD) is a well-established non-destructive technique that utilises the phenomenon of coherent X-ray scattering to extract atomic and molecular structural information [1]. XRD is chiefly used for identification of crystalline materials but has also been shown to have promise in the analysis of biological tissue [2]. In a technique similar to transmission X-ray computed tomography (CT), data collected from multiple angular positions can be used to reconstruct a cross-sectional slice or a whole 3D volume that can be used to identify regions with varying atomic or molecular structure within the sample [3]. Using pre-determined XRD signatures, this data can also be used to identify unknown materials within the sample [4].

Traditionally, XRD techniques employ an angular-dispersive approach, where a monochromatic pencil beam is incident upon the sample and the scattering intensity is measured as a function of the scattering angle. In most cases, XRDCT systems employ a similar method, often using synchrotron radiation. Synchrotron based XRDCT systems have shown to be effective and have been used for biological imaging and identifying crystalline compounds [1,5,6]. However, limited access to synchrotron facilities renders this technique inaccessible and costly for mainstream applications. Alternatively, a conventional X-ray generator can be used with appropriate filtration to produce a quasi-monochromatic beam [7]. However, this is very inefficient resulting in a low incident beam flux. This, coupled with the low probability of coherent scatter (compared to other possible interactions) results in a very weak XRD signal, increasing the acquisition time. This paper describes further development of the pixelated X-ray diffraction, PixD, technique which utilises a large area energy-dispersive detector with a broad X-ray source spectrum to significantly reduce acquisition times compared to conventional approaches [8]. Application of PixD to XRDCT could make it a viable method for rapid spatially resolved material analysis, with applications in security screening, clinical pathology and industrial quality control.

2.   PixD system

2.1.   HEXITEC detector

Key to the PixD technique is the HEXITEC pixelated energy-dispersive detector which is capable of providing a full energy histogram in every pixel [9]. The active sensor material is a single cadmium telluride (CdTe) crystal, measuring $20 \times 20 \times 1$ mm, consisting of 80×80 individual pixels (total 6400) on a 250 μm pitch. The CdTe crystal was maintained at 12 °C by means of a Peltier cooling module. During a measurement the CdTe crystal was subject to a bias voltage of −475 V which was cycled at the end of each acquisition (never more than 250 s) to avoid polarisation and degraded sensor performance [10].

One of the drawbacks of pixelated detectors is the effect known as charge sharing, in which the electron cluster from a single X-ray interaction event can be read by multiple neighbouring pixels, resulting in the X-ray energy incorrectly read as multiple lower energy X-rays [11]. Without correction, these events can lead to a degradation of the spectroscopic performance of the detector by introducing a significant background of low energy events, resulting in a reduction in the signal-to-noise ratio (SNR) in XRD profiles obtained from the raw data. To minimise this, the detector was operated in charge sharing discrimination (CSD) mode where events recorded in adjacent pixels are rejected. A frame rate of 998 Hz was used during these experiments, with a detector readout time of 1 ms.

2.2.   Combining data from all pixels

Small pixel detectors often suffer from inter-pixel variations in gain caused by inclusions and defects within the crystal structure, resulting in shifts in individual energy spectra [12]. Therefore, an energy calibration curve was obtained for each pixel following a previous study [13] using a radioisotope source (Am-241 with gamma emissions at 13.9, 17.8, 20.8 and 59.5 keV). This curve was used to convert channel numbers into energy bins (E) of width 0.25 keV, with 400 channels covering an energy range of 0 to 80 keV. Every pixel was then assigned a scattering angle (θ) using knowledge of the source-sample-detector geometry. The energy spectrum in each pixel was converted to momentum transfer (x) via Eq. (1). This common axis allows the data from all pixels to be summed in a hybrid angular- and energy-dispersive technique.

$$x = \frac{E}{hc} \sin\left(\frac{\theta}{2}\right) \ , \tag{1}$$

2.3.   Fly-scan technique: continuous sample motion during acquisition

Generally, XRDCT systems employ a step-scan technique where the sample is moved to position, exposed to X-rays and the detector's response is recorded. The sample is then moved a translation step of predefined size and the process is repeated [3,14–16]. During our experiments the translation steps were set to 1 mm with an acquisition time of 5 s per step and an angular step of 1°, covering the full 360° angular range. With a sample diameter of 30 mm, this technique resulted in an output of 10,800 files containing the individual momentum transfer spectra.

To reduce the total acquisition time, a fly-scan technique was also employed, during which the sample was moved at a constant speed of 0.2 mms^{-1}, equating to the same X-ray exposure per mm as the step-scan technique (i.e. 5 s per mm), allowing for like-for-like comparison between the two techniques. During the continuous translation of the sample, the detector was collecting data without pause, only stopping when the sample reached the end of the translational pass, allowing the sample to rotate and return to its original location to begin another pass. The detector bias was also refreshed at this point. This technique resulted in 360 files, each containing 149,700 frames (framerate of 998 Hz × acquisition time of 150 s). As the framerate and sample speed are known, information about the translational location of each measurement, can be determined directly from the frame number.
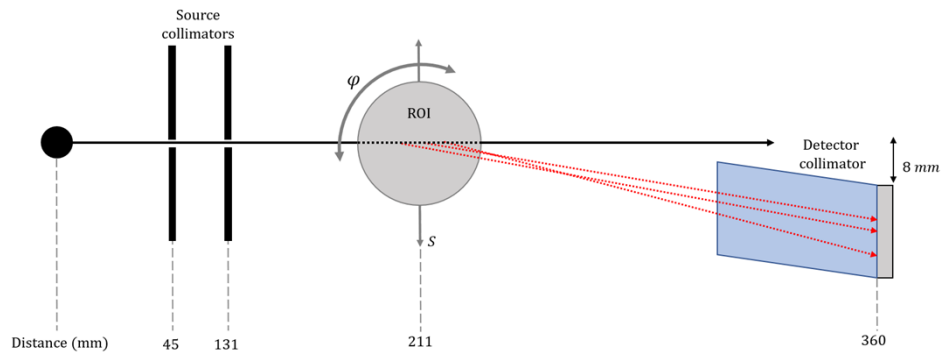
Fig. 1. Schematic diagram of the experimental setup used to collect XRD projections.

2.4. Experimental benchtop XRDCT setup

The major components of this benchtop XRDCT setup are illustrated in Fig. 1, which include a compact X-ray generator (SB-80-1 K, Source-Ray Inc., U.S.A.), source collimation, a test sample at the isocentre, detector collimation and a HEXITEC detector to record the scattered X-rays. The photon flux of the X-ray generator is estimated to be 1.4×10^6 photons/mm^2 at 100 cm from the source. This was calculated using the SPEKTR 3.0 toolkit [17]. The primary X-ray beam was collimated using two 2 mm pinhole lead masks (3 mm thick) to create a 2.2 mm-diameter spot on the rotation plane.
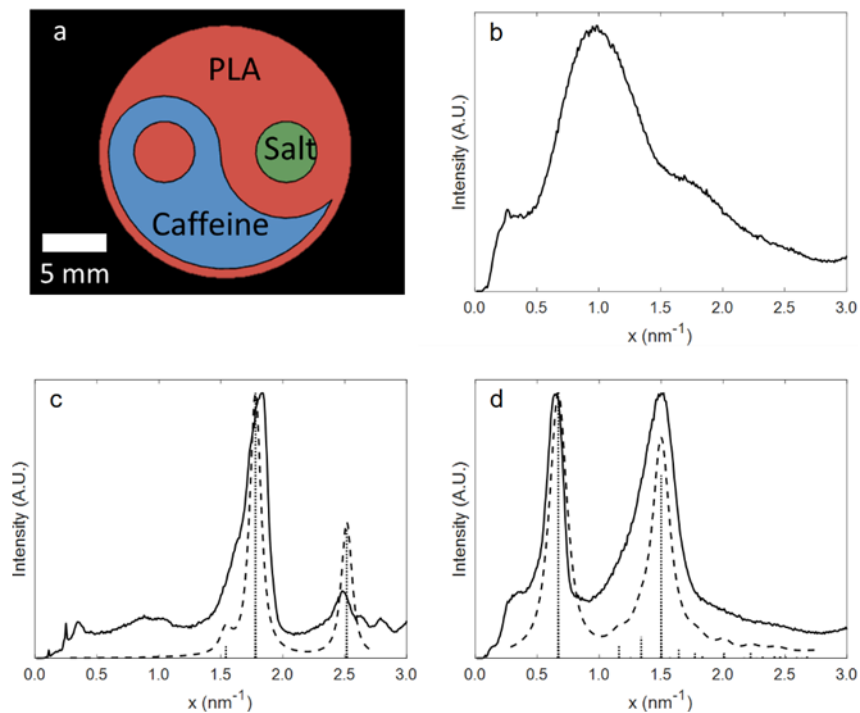

Fig. 2. (a) Schematic of test sample and measured XRD profiles (solid lines) for: (b) PLA, (c) salt and (d) caffeine. Database values (dotted vertical lines) and simulated broadened profiles (dashed lines) shown for salt and caffeine.

The diameter of the incoming beam introduced an inherent uncertainty in the location of the scattering events, affecting both the spatial and momentum transfer resolutions. To minimise this, the sample was moved close to the source collimators to reduce the effect of divergence of the beam. The beam diameter was measured using a small pixel (49.5 μm) flat panel detector (1215A, Rayence, South Korea), and ranged from 2.06 mm to 2.41 mm in a region of interest (ROI, see Fig. 1), 25 mm either side of the centre of rotation. To minimise the detection of transmitted X-rays, a detector side collimator was designed and 3D printed using bronze infused polylactic acid (PLA) filament (Ultimaker, Netherlands). The detector was also offset by 8 mm.

Figure 2(a) shows the design of the test sample used, which was 3D printed using standard PLA filament and the two cavities were filled with table salt (sodium chloride) and caffeine. Figure 2(b-d) shows the XRD profiles for these materials measured in isolation. In this case the samples were 5 mm thick, and data were collected for 60 s. The XRD profile for PLA exhibits a broad diffraction peak centred at $0.98\,\mathrm{nm}^{-1}$, consistent with other reported values obtained using ADXRD [18,19]. The absence of characteristic peaks indicates the structure of PLA is amorphous. The XRD profiles of caffeine and salt are compared to database values [20]. The database values are given in 2θ and intensity pairs, which were converted to momentum transfer via Eq. (1) and are represented in Fig. 2 as stems. To more accurately match the collected data, broadened profiles were simulated by calculating Gaussians at each database position and summing them together, shown in Fig. 2 (dashed lines).

2.5. Tomographic reconstruction

As we use a pencil beam geometry, the reconstruction can be treated as a conventional parallel beam computed tomography problem. However, the dimensionality of the data is increased by
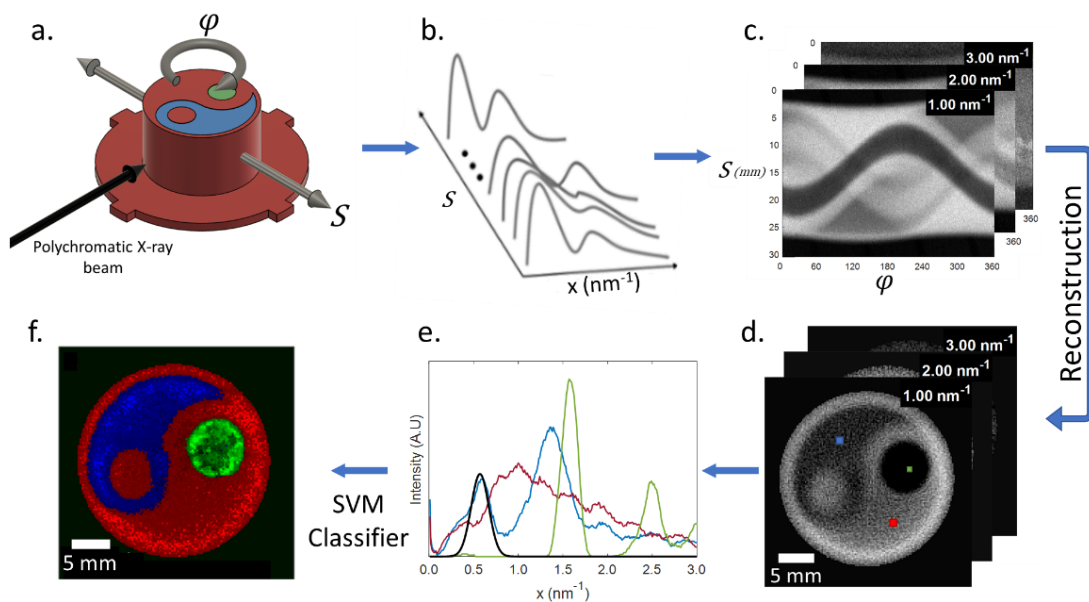

Fig. 3. Data acquisition and reconstruction process. (a) Incoming polychromatic (white) X-ray beam illuminating sample (b) XRD profiles recorded for each position (c) Momentum transfer data used to produce sinograms. (d) Reconstructed tomographic images are stored in 3D matrix. (e) XRD profiles produced by taking line profile in 3rd dimension (momentum transfer) of matrix. Solid black line shows Gaussian fitted to caffeine peak for momentum transfer resolution analysis. (f) Material characterisation using trained SVM classifier.

one dimension (momentum transfer, x) with respect to conventional transmission CT. Together with the two spatial dimensions (position, s and rotation angle, φ) of a single slice CT acquisition scheme, a three-dimensional data set (s, φ, x) was gathered, containing sinograms at 0.01 nm^{-1} intervals. Reconstruction of the sinograms yields a set of two-dimensional tomographic images at each momentum transfer value, allowing for material characterisation of each pixel by taking a line profile in the 3rd axis, extracting the reconstructed XRD profiles. A summary of the process is shown in Fig. 3. Reconstruction was carried out in MATLAB using a modified Feldkamp-David-Kress (FDK) algorithm for parallel beam geometry [21].

3. Results

3.1. Data binning – Spatial resolution versus material characterisation confidence

As described in section 2.3, the fly-scan method results in files containing a very large number of frames (149,700). With each frame containing an average of only 45 counts, analysis of a single frame would result in very noisy XRD profiles; i.e. there is insufficient signal to recover atomic and/or molecular structural information in a single frame. Therefore, data were binned to improve the SNR in the resulting XRD profiles. However, as the sample is in continuous motion, binning data from a greater number of frames results in a deterioration in the spatial resolution, due to the mixing of data from a greater volume of the sample. For example, data binned from 997 frames (from here on referred to as bin width of 1 s due to the frame rate of 997 Hz), results in the mixing of data collected from the beam diameter + 0.2 mm, as this is the distance moved in 1 s, whereas a bin width of 5 s results in a mixing of data from beam diameter + 1 mm.

3.2. Total scan time

The conventional step-scan method resulted in a total scan time of 29 hrs. This was reduced to 16.8 hrs by using our fly-scan method, a reduction of 42%. During both procedures, the actual time where useful data were being collected was 15 hrs, equating to a dead time of 48% for the step-scan method and 11% for the fly-scan method. The main sources of dead time were the time taken to move the sample to the new position and the automatic bias refreshing which takes place at the end of each acquisition. Continuous movement reduces the contribution of these two factors as the data is collected during the movement and bias refreshing is only carried out at the end of each lateral translation, and not at each 1 mm interval.

3.3. Analysis of spatial resolution

The imaging performance of the system is best characterized by the spatial resolution, which describes how far two features of an object need to be separated by to be distinguishable in the reconstructed image [22]. To compare the spatial resolution, reconstructed images were summed over all momentum transfer values to produce a single image. The data from the fly scan method was then binned to allow for a direct comparison between the results obtained from the two methods. Determining the spatial resolution can be done using well-known techniques employed in conventional X-ray CT imaging such as measurement of the modulation transfer function (MTF) which require special test samples [23,24]. In this paper, we are interested in a direct comparison between the two scanning techniques, so a simpler knife-edge method was used [25–27]. An intensity profile was taken over the sharp edge of the sample container (indicated by the red line in Fig. 4(a)), obtaining the edge spread function (ESF) by fitting a Sigmoid to the pixel values. The point spread function (PSF) was then calculated using the ESF and fitted with a Gaussian that was used to determine the full-width-at-half-maximum (FWHM) of the PSF as shown in Fig. 4(b).

Changing the duration over which the data are binned has the effect of changing the reconstructed image pixel size. This does not necessarily improve the spatial resolution, which is predominately
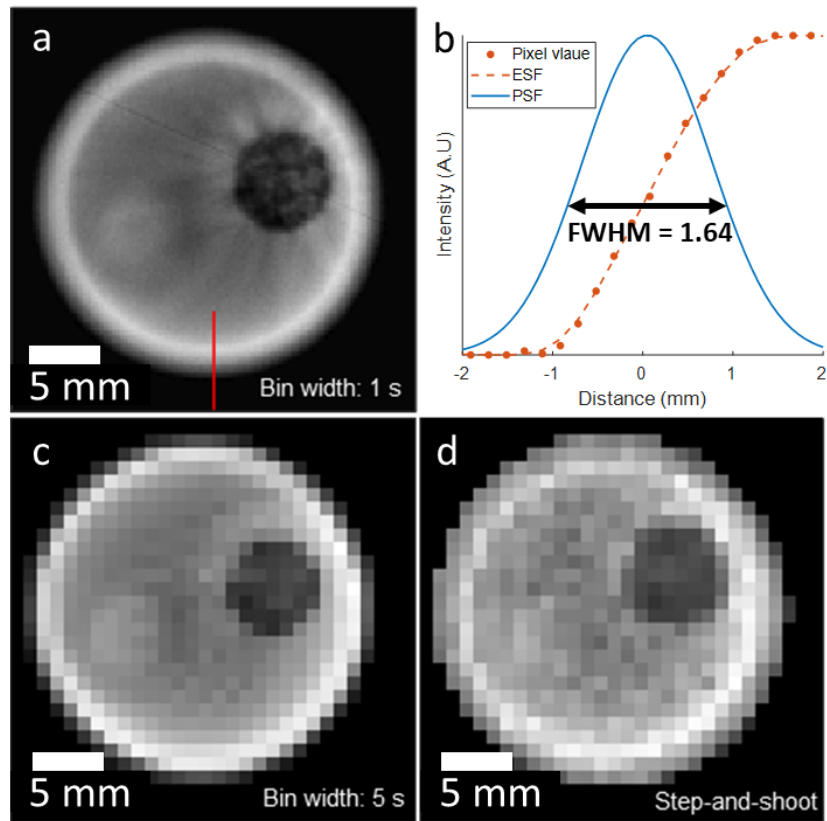
Fig. 4. (a-b) Method for estimation of spatial resolution showing the fitted edge spread function (ESF) and Gaussian fitted to point spread function (PSF). Example shows FWHM obtained for reconstructed image using the fly-scan technique – binned over 1 s. At a speed of 0.2 mms^{-1}, binning data over 5 s equates to a translation of 1 mm, which is the step size used for the step-scan method. This allows for direct comparison of data obtained using the two techniques (c) and step-scan technique (d).

limited by the relatively large beam diameter. As such, we expect the spatial resolution to be no smaller than the diameter of the beam. However, as the results in Table 1 show, the data collected using the continuous motion seems to result in images with improved resolution. This is due to a phenomenon known as super-resolution (SR) [28]. Generally SR techniques utilise subpixel sized steps in front of the detector to produce images of higher resolution than possible with a single acquisition [29,30] . In this case, as the limiting factor is the diameter of the incoming beam, the small step sizes relative to the beam diameter have the same effect. This technique is limited by the low count when the bin width is short, reducing the signal-to-noise ratio and ultimately impairing the spatial resolution. Therefore, there is an optimal bin width that results in the best spatial resolution – 3.0 s in this case.

3.4. Momentum transfer resolution

When converting the energy spectra from individual pixels to XRD profiles via Eq. (1), the scattering angle θ is determined by assuming all scattered X-rays originate from the centre of the sample and interact with the centre of the pixel. However, the sample thickness, beam diameter, pixel pitch and location of the pixel relative to the centre of the sample all contribute to an error
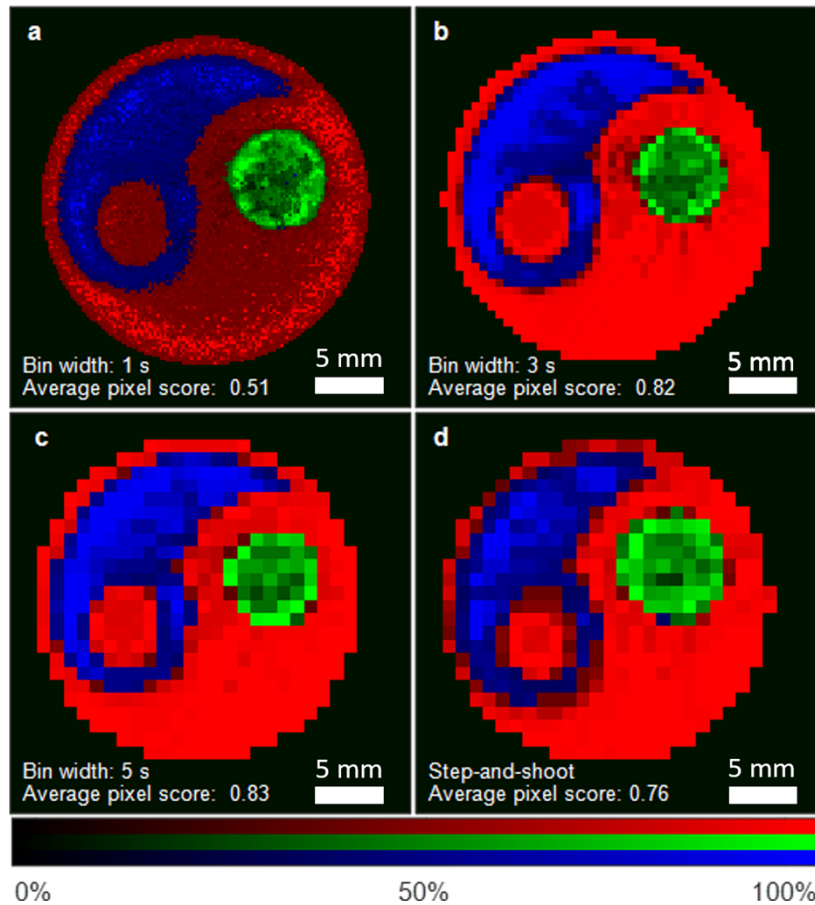
Fig. 5. Material classification using trained classifier, showing the effect of bin width on classification scores for data obtained using fly-scan technique (a-c) and step-scan technique (d). Regions indicated as red, blue and green have been classified as PLA, caffeine and salt respectively.

Table 1. Spatial and momentum transfer resolution analysis and average SVM pixel score

Bin width (s)	1.0	2.0	3.0	4.0	5.0	SS[a]
Pixel pitch (mm)	0.2	0.4	0.6	0.8	1.0	1.0
FWHM (mm) spatial	1.64	1.55	1.51	1.76	1.92	2.12
FWHM (nm^{-1}) momentum transfer	0.22	0.22	0.22	0.22	0.22	0.22
Average pixel SVM score	0.51	0.78	0.82	0.83	0.83	0.76

[a]Data collected using step-scan method.

in the scattering angle. Taking this into account, our calculated scattering angles have an average error of $\pm 0.38°$ when using a sample of thickness 5 mm. This equates to an error of $\pm 0.04\,nm^{-1}$ in momentum transfer space using 0.25 keV energy bins and $\pm 0.06\,nm^{-1}$ when energy bin size is increased to 0.50 keV. The XRD profiles produced by direct measurement (Fig. 2(b-d)) and reconstructed XRD profiles (Fig. 3(e)) were analysed by fitting a Gaussian to the first caffeine

peak ($0.67\,\text{nm}^{-1}$) and calculating the FWHM, demonstrated by the solid black line in Fig. 3(e). The direct measurement of caffeine of thickness 5 mm resulted in a FWHM of $0.16\,\text{nm}^{-1}$, while the reconstructed XRD profiles all produced a FWHM of $0.22\,\text{nm}^{-1}$ for all bin sizes used; 1–5 seconds. This was the same for the step-scan technique.

The momentum transfer resolution of the system is dependent on various factors, most significantly the geometry of the setup. Increasing the sample-to-detector distance will result in a smaller error in the calculated scattering angles, improving the overall momentum transfer resolution. However, this comes at the cost of reducing the overall solid angle covered by the detector, increasing the total scan time. When scan duration is not a limitation, such as a single direct measurement, the system can quickly be optimised for improved momentum transfer resolution.

3.5. Material classification

Material classification of the reconstructions was performed on MATLAB using support vector machines (SVMs), which construct optimised hyperplanes to discriminate XRD profiles into four material classes [31]. Training was carried out using XRD profiles produced by samples of thickness ranging from 0.5-10 mm, randomly positioned ±25 mm from the isocentre and with acquisition times ranging from 1-30 s. The trained SVMs were then applied to classify the reconstructed XRD profiles. Pixels were assigned to the material class that yielded the highest score. The material classification maps obtained can be seen in Fig. 5. For convenience of comparison, the SVM score is transformed to a probabilistic output and visualised by the brightness of the pixel, with brighter pixels indicating a higher SVM score and, therefore, higher confidence in the classification.

As expected, when the bin width is small, the lower count results in a lower average SVM score. However, binning the data over periods longer than 2 s shows little improvement in the SVM scores, as shown in Table 1. This indicates a limitation in the trained classifier, which may be improved with larger training dataset. A direct comparison between the step-scan technique and the equivalently binned data from the fly-scan method shows an increase in the SVM scores. This is most likely due to the improved spatial resolution which results in less mixing of signals from neighbouring parts of the sample. However, further work is required to better understand the effects of the continuous motion on the momentum transfer signals.

4. Discussion

The key challenge in the development of a practical benchtop XRDCT system has been the relatively long scan times. As shown in (1), the technique requires knowledge of the scattering angle and energy. While there has been some work done on the use of collimation and coded apertures to allow for the use of a fan or cone beams [32–34], the most widely used approach to define the scattering angle is the use of a pencil beam geometry. The energy of the scattered X-rays can be determined using an energy dispersive detector or set by using a monochromatic source. Using a conventional energy dispersive X-ray detector necessitates collimation on the detector side to reduce the error in the angle measurement. The small detection area results in very long acquisition times making this approach to XRDCT impractical. Alternatively, a large flat panel detector can be used when the incoming beam is monochromatic. This can be done with a quasi-monochromatic source [7] which can be achieved using filtration. However, this results in a significant reduction in the beam intensity which increases the acquisition time, in addition to introducing an error in the energy value. In practice, the most effective XRDCT systems employ bright, highly monochromatic synchrotron radiation with a fast, large area detector system [35–38]. The focus of the current investigation was therefore to negate the need for synchrotron radiation by using a commercially available 2D pixelated spectroscopic detector and a cheap and widely available polychromatic X-ray generator. In essence, the current study

represents a novel approach to XRDCT which is relatively easy to implement in a typical X-ray lab and even more significantly, it is scalable.

While the practical setup of the system allows for quick alterations that can change the performance of the system, such as the size of the pinhole collimator, the fly-scan data acquisition technique demonstrated allows for greater freedom in the analysis of the data. In this study, we demonstrated the ability to determine the optimal bin width for the best spatial resolution. However, software limitations meant that the minimum acquisition window was 1 s, allowing for binning of data only in multiples of seconds. Spatial resolution can be further optimised if non-integer second bin widths could be implemented.

Analysis of the momentum transfer resolution of the reconstructed XRD profiles did not show a deterioration at higher spatial resolutions, i.e. when data were binned over a shorter duration. This was surprising as summing data over a shorter duration reduced the average SVM confidence score. This suggests that the SVM training has not been optimised. The SVMs were trained using XRD profiles produced by direct measurements. Using XRD profiles obtained by means of reconstruction of XRDCT data may help to improve material classification. Currently the system can only classify materials that have previously been scanned for SVM training. Producing simulated broadened XRD profiles from database data could potentially be used to train SVMs for classifying a wide range of materials.

The scalability of this system is also very promising. The source used for this study was operated at the maximum power of 80 W, which is relatively low. While this highlights the potential for a portable system in the future, widely available lab based X-ray sources are much more powerful and their use can significantly reduce the total scan time. In addition to this, multiple detectors can be used simultaneously to further reduce the total scan time. This is particularly promising as there have been recent advances in a 2×2 tiled HEXITEC system [37] which has 4 times the detection area of a single HEXITEC detector, potentially reducing the total scan time 4-fold.

5. Conclusion

In this investigation, we demonstrated a novel benchtop hybrid energy and angular dispersive XRDCT method, using a fly-scan scan technique, and examined its performance by classifying materials in a test sample using their reconstructed XRD profiles. A like-for-like comparison of our technique to the established step-scan technique showed an improvement in the spatial resolution of the reconstructed images, from 2.12 mm to 1.51 mm, while reducing the total scan time from 29 hrs to 16.8 hrs. Our technique also shows improvement in the classification of materials, with an increase in the average SVM confidence score, from 0.76 to 0.83. The scalability of this technique means that future systems can be improved on, simply by using a more powerful source, smaller beam diameter and/or multiple detectors. Overall, the results and findings from this study should be considered for the design of benchtop XRDCT systems adopting a pixelated detector system.

Disclosures. The authors declare no conflicts of interest.

Data availability. The data underlying the results presented in this paper are not publicly available at this time but may be obtained from the authors upon reasonable request.

References

1. A. A. Bunaciu, E. G. Udriştioiu, and H. Y. Aboul-Enein, "X-Ray Diffraction: Instrumentation and Applications," Crit. Rev. Anal. Chem. **45**(4), 289–299 (2015).
2. R. M. Moss, A. S. Amin, C. Crews, C. A. Purdie, L. B. Jordan, F. Iacoviello, A. Evans, R. D. Speller, and S. J. Vinnicombe, "Correlation of X-ray diffraction signatures of breast tissue and their histopathological classification," Sci. Rep. **7**(1), 12998 (2017).

3. R. M. Moss, M. D. Wilson, E. J. Morton, and R. D. Speller, "Hybrid Angular-and Energy-Dispersive X-ray Diffraction Computed Tomography," in *Proceedings of IEEE Nuclear Science Symposium and Medical Imaging Conference (NSS/MIC)* (IEEE, 2018), pp. 1–3.

4. E. Cook, R. Fong, J. Horrocks, D. Wilkinson, and R. Speller, "Energy dispersive X-ray diffraction as a means to identify illicit materials: A preliminary optimisation study," Appl. Radiat. Isot. **65**(8), 959–967 (2007).

5. J. Srodon, "X-ray powder diffraction identification of illitic materials," Clays Clay Miner. **32**(5), 337–349 (1984).

6. R. Das, E. Ali, and S. B. Abd Hamid, "Current applications of x-ray powder diffraction - a review," Rev. Adv. Mater. Sci. **38**(2), 95–109 (2014).

7. Z. Zhu, A. Katsevich, A. J. Kapadia, J. A. Greenberg, and S. Pang, "X-ray diffraction tomography with limited projection information," Sci. Rep. **8**(1), 522 (2018).

8. D. O'Flynn, C. Crews, I. Drakos, C. Christodoulou, M. Wilson, M. Veale, P. Seller, and R. Speller, "Materials identification using a small-scale pixellated x-ray diffraction system," J. Phys. D: Appl. Phys. **49**(17), 175304 (2016).

9. L. Jones, P. Seller, M. Wilson, and A. Hardie, "HEXITEC ASIC—a pixellated readout chip for CZT detectors," Nuclear Instruments and Methods in Physics Research Section A: Accelerators, Spectrometers, Detectors and Associated Equipment **604**(1-2), 34–37 (2009).

10. M. C. Veale, J. Kalliopuska, H. Pohjonen, H. Andersson, S. Nenonen, P. Seller, and M. D. Wilson, "Characterization of M-π-n CdTe pixel detectors coupled to HEXITEC readout chip," J. Instrum. **7**(01), C01035 (2012).

11. M. C. Veale, S. J. Bell, D. D. Duarte, A. Schneider, P. Seller, M. D. Wilson, and K. Iniewski, "Measurements of charge sharing in small pixel CdTe detectors," Nuclear Instruments and Methods in Physics Research Section A: Accelerators, Spectrometers, Detectors and Associated Equipment **767**, 218–226 (2014).

12. J. Scuffham, M. C. Veale, M. D. Wilson, and P. Seller, "Algorithms for spectral calibration of energy-resolving small-pixel detectors," J. Instrum. **8**(10), P10024 (2013).

13. P. Seller, S. Bell, R. J. Cernik, C. Christodoulou, C. K. Egan, J. A. Gaskin, S. Jacques, S. Pani, B. D. Ramsey, C. Reid, P. J. Sellin, J. W. Scuffham, R. D. Speller, M. D. Wilson, and M. C. Veale, "Pixellated Cd(Zn)Te high-energy X-ray instrument," J. Instrum. **6**(12), C12009 (2011).

14. S. Pani, E. J. Cook, J. A. Horrocks, J. L. Jones, and R. D. Speller, "Characterization of breast tissue using energy-dispersive X-ray diffraction computed tomography," Appl. Radiat. Isot. **68**(10), 1980–1987 (2010).

15. P. Bleuet, E. Welcomme, E. Dooryhée, J. Susini, J.-L. Hodeau, and P. Walter, "Probing the structure of heterogeneous diluted materials by diffraction tomography," Nat. Mater. **7**(6), 468–472 (2008).

16. G. Harding, J. Kosanetzky, and U. Neitzel, "X-ray diffraction computed tomography," Med. Phys. **14**(4), 515–525 (1987).

17. J. Punnoose, J. Xu, A. Sisniega, W. Zbijewski, and J. H. Siewerdsen, "Technical Note: spektr 3.0-A computational tool for x-ray spectrum modeling and analysis," Med. Phys. **43**(8Part1), 4711–4717 (2016).

18. V. S. G. Silverajah, N. Ibrahim, W. Yunus, H. Hassan, and B. W. Chieng, "A Comparative Study on the Mechanical, Thermal and Morphological Characterization of Poly(lactic acid)/Epoxidized Palm Oil Blend," Int. J. Mol. Sci. **13**(5), 5878–5898 (2012).

19. M. Hassan, I. Mustapa, N. Daud, N. H. N. Sudin, A. Majhool, and E. Mahmoudi, "Improvement Thermomechanical Properties of Polylactic Acid via Titania Nanofillers Reinforcement," J. Adv. Res. Fluid Mech. Thermal Sci. **70**(1), 97–111 (2020).

20. F. H. Allen, "The Cambridge Structural Database: a quarter of a million crystal structures and rising," Acta Crystallogr B **58**(3), 380–388 (2002).

21. L. A. Feldkamp, L. C. Davis, and J. W. Kress, "Practical cone-beam algorithm," J. Opt. Soc. Am. A **1**(6), 612–619 (1984).

22. E. C. McCullough, J. T. Payne, J. Hillier, L. Baker, R. R. Hattery, P. F. Sheedy, D. H. Stephens, and E. Gedgaudus, "Performance Evaluation and Quality Assurance of Computed Tomography Scanners, with Illustrations from the EMI, ACTA, and Delta Scanners," Radiology **120**(1), 173–188 (1976).

23. J. Rueckel, M. Stockmar, F. Pfeiffer, and J. Herzen, "Spatial resolution characterization of a X-ray microCT system," Appl. Radiat. Isot. **94**, 230–234 (2014).

24. E. Samei, M. J. Flynn, and D. A. Reimann, "A method for measuring the presampled MTF of digital radiographic systems using an edge test device," Med. Phys. **25**(1), 102–113 (1998).

25. T. Allen, O. Olumide, E. Zhang, and P. Beard, "Large area laser scanning optical resolution photoacoustic microscopy using a fibre optic sensor," Biomed. Opt. Express **9**(2), 650 (2018).

26. K. Sato, Y. Hasegawa, K. Kondo, K. Miyazaki, T. Matsushita, and Y. Amemiya, "Development of a high-resolution x-ray imaging system with a charge-coupled-device detector coupled with crystal x-ray magnifiers," Rev. Sci. Instrum. **71**(12), 4449–4456 (2000).

27. Q. Chen, T. Jin, W. Qi, X. Mo, and L. Xi, "Label-free photoacoustic imaging of the cardio-cerebrovascular development in the embryonic zebrafish," Biomed. Opt. Express **8**(4), 2359 (2017).

28. A. M. Tekalp, M. K. Ozkan, and M. I. Sezan, "High-resolution image reconstruction from lower-resolution image sequences and space-varying image restoration," in *Proceedings of IEEE International Conference on Acoustics, Speech, and Signal Processing* (IEEE, 1992), pp. 169–172.

29. R. R. Schultz and R. L. Stevenson, "Extraction of high-resolution frames from video sequences," IEEE Trans. on Image Process. **5**(6), 996–1011 (1996).

30. M. Ben-Ezra, A. Zomet, and S. K. Nayar, "Video super-resolution using controlled subpixel detector shifts," IEEE Trans. Pattern Anal. Mach. Intell. **27**(6), 977–987 (2005).

31. C. Cortes and V. Vapnik, "Support-vector networks," Machine learning **20**(3), 273–297 (1995).

32. A. Harding, J.-P. Schlomka, and G. L. Harding, "Simulations and experimental feasibility study of fan-beam coherent-scatter CT," Proc. SPIE **4786**, 202 (2002).

33. Z. Zhu, R. A. Ellis, and S. Pang, "Coded cone-beam x-ray diffraction tomography with a low-brilliance tabletop source," Optica **5**(6), 733–738 (2018).

34. S. Pang, M. Hassan, J. Greenberg, A. Holmgren, K. Krishnamurthy, and D. Brady, "Complementary coded apertures for 4-dimensional x-ray coherent scatter imaging," Opt. Express **22**(19), 22925–22936 (2014).

35. G. Artioli, T. Cerulli, G. Cruciani, M. C. Dalconi, G. Ferrari, M. Parisatto, A. Rack, and R. Tucoulou, "X-ray diffraction microtomography (XRD-CT), a novel tool for non-invasive mapping of phase development in cement materials," Anal. Bioanal. Chem. **397**(6), 2131–2136 (2010).

36. A. A. Hendriksen, M. Bührer, L. Leone, M. Merlini, N. Vigano, D. M. Pelt, F. Marone, M. di Michiel, and K. J. Batenburg, "Deep denoising for multi-dimensional synchrotron X-ray tomography without high-quality reference data," Sci. Rep. **11**(1), 11895 (2021).

37. L. Jowitt, M. Wilson, P. Seller, C. Angelsen, R. M. Wheater, B. Cline, D. Schöne, F. Lauba, M. Goede, R. Ball, M. Verhoeven, G. Gottseleben, M. N. Boone, F. Van Assche, and M. C. Veale, "HEXITEC 2 × 2 tiled hard X-ray spectroscopic imaging detector system," J. Instrum. **17**(01), P01012 (2022).

38. H. Iwamoto, "Synchrotron Radiation X-ray Diffraction Techniques Applied to Insect Flight Muscle," Int. J. Mol. Sci. **19**(6), 1748 (2018).